Bio-inspired pneumatic shape morphing elastomers

Emmanuel Siéfert, Etienne Reyssat, José Bico, Benoit Roman

Bio-inspired pneumatic shape morphing elastomers

Emmanuel Siéfert[1], Etienne Reyssat[1], José Bico[1], Benoit Roman[1]*

[1]Laboratoire de Physique et Mécanique des Milieux Hétérogènes,
CNRS, ESPCI Paris, PSL Research University, 10 rue Vauquelin, 75005 Paris, France,
and Sorbonne Université, Université Paris Diderot

* benoit.roman@espci.fr.

Shape-morphing structures are at the core of future applications in aeronautics [1], minimally invasive surgery [2], tissue engineering [3] or smart materials [4]. Current engineering technologies, based on inhomogeneous actuation across the thickness of slender structures, are however intrinsically limited to one-directional bending [5]. Here, we describe a strategy where mesostructured elastomer plates undergo fast, controllable and complex shape transformations under applied pressure. Similarly to pioneering techniques based on soft hydro- gel swelling [6–10], these pneumatic shape morphing elastomers, termed here as baromorphs, are inspired by the morphogenesis of biological structures [11–15]. Geometric restrictions are overcome by controlling precisely the local growth rate and direction through a specific network of airways embedded inside the rubber plate. We show how arbitrary 3D shapes can be programmed using an analytic theoretical model, propose a direct geometric solution to the inverse problem and illustrate the versatility of the technique with a collection of configurations.

Morphing a thin plate into a programmed shape is a challenging problem, highlighted by Gauss: if the distances along the surface are not modified, the Gaussian curvature cannot be changed and only a limited family of 3D surfaces is achievable, as commonly observed with bilayer sheets[16,17]. However, Nature overflows with examples of geometrically complex thin objects, such as leaves or organs epithelia [11]. For instance, differential growth induces the elegant shape of flower petals [12], or may conversely crinkle an initially flat leave when the growth rate is deregulated [13]. While the growth process may be spatially homogeneous, the orientations of cellulose fibres may also induce anisotropic growth, which leads to the hygroscopic actuation of wheat awns[14] or to the chiral shape of some seed pods[15].

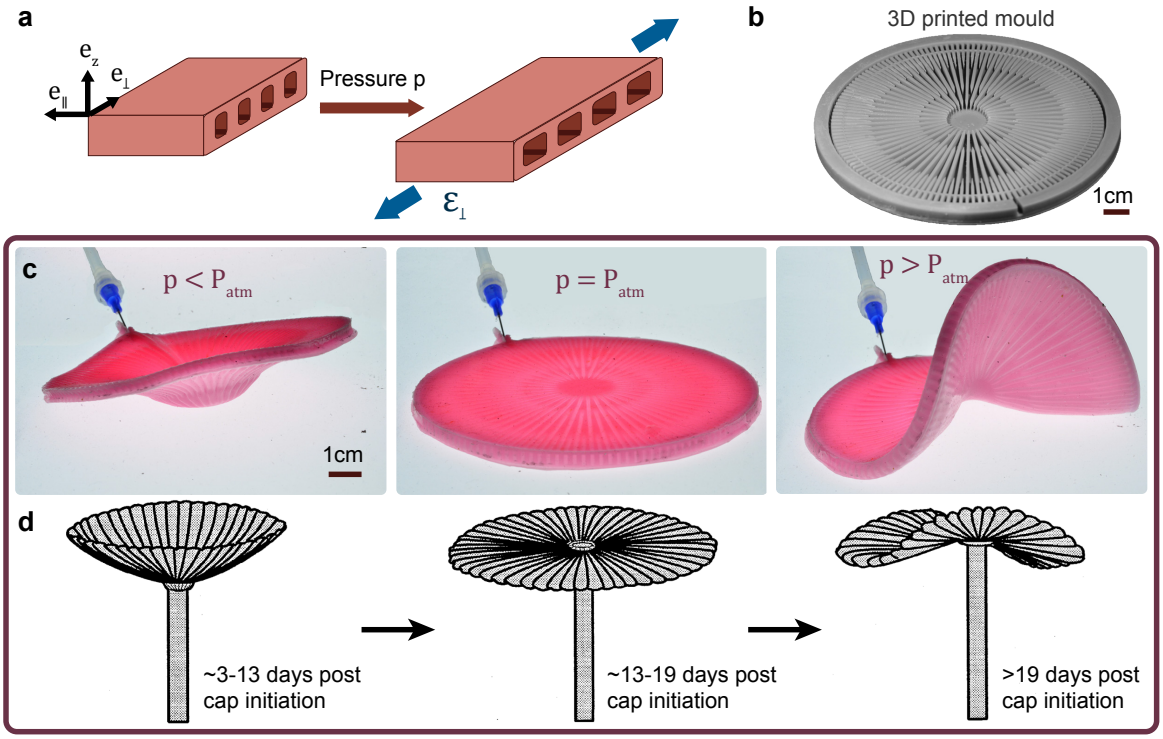

Figure 1: Principle of pressure actuated baromorph plate. **a**, Schematic of actuation: the pressure inside the airways induces anisotropic inflation of the plate (higher strain normal to the airways than along the channels). **b**, 3D printed mould used to cast the baromorph illustrated in panel c. **c**, Actuation of the plate: suction (left) tends to contract the plate in the azimuthal direction, leading to a bowl (positive Gaussian curvature), while inflation (right) leads to an excess angle and a transformation into a saddle shape (negative Gaussian curvature). **d**, Evolution of the cap of an *acetabularia* alga from a bowl to a saddle shape due to a preferential growth in the azimuthal direction (adapted from Serikawa *et al.* [18])

Inspired by biological morphogenesis, pioneering experiments have been carried out with hydrogel plates where the inhomogeneous isotropic [6,7,19] or anisotropic [9,10] swelling properties

were spatially distributed in order to obtain various 3D shapes once immersed in a bath of hot water. Nevertheless, the experimental realisations developed so far involve slow diffusive swelling processes and very soft objects that generally cannot sustain their own weight. In contrast, pneumatic actuation presents strong advantages such as large work load, reversibility, controllability and fast actuation, which have led to the recent development of multiple soft robotics actuators for twisting, contracting, expanding or bending motions [20]. However, such actuators generally rely on bilayers [5] or are limited to surface texturing effects [21], which imposes strong constraints on the achievable states. Our approach bridges these two emerging fields, bio-inspired shape-morphing and pneumatic soft robotics, with a new easy-to-build, easy-to-control object, referred to as a baromorph.

Baromorphs consist in elastomer plates embedding a network of airways (see Methods for fabrication details), which give rise to a programmed family of shapes upon air inflation or suction. Such structures can be viewed as pneumatic metamaterials[22]. When the inner pressure is increased (or decreased), the elongated channels tend to inflate (or deflate) anisotropically [23]: The length of an inflated channel remains almost unchanged, while its width increases (Fig. 1a). This anisotropy results in a controllable modification of the effective rest-lengths of the baromorph, mimicking the anisotropic growth of a biological tissue, with a magnitude that depends on the geometry of the inner channels and on the applied pressure. The plate deforms according to the new target metric imposed by the network of airways, and may buckle out of plane to reach an equilibrium 3D shape that minimises the total elastic energy - sum of stretching and bending energies.

In Fig. 1c, we illustrate the deformation of a baromorph plate with radial channels obtained by casting the 3D printed template shown in Fig. 1b: the target expansion is mainly circumferential. Upon suction and consequent azimuthal contraction, the plate adopts a bowl shape (with positive Gaussian curvature). Conversely, inflation induces an azimuthal expansion and leads to an excess angle in the plate, which destabilises into a surface of negative Gaussian curvature. These transformations are reminiscent of the morphing evolution of *Acetabularia* (Figure

1d)[11,18]. After initiation, the cap of this unicellular alga evolves from a bowl to a flat and eventually to a saddle shape, essentially for the same reason as our baromorph: biological growth in the cap is stronger in the circumferential direction than along the radius.

A first step in understanding and programming a baromorph is to predict the local deformation of airways in absence of external geometrical constraints, i.e. the target in-plane strains orthogonal $\varepsilon^t_\perp$ and parallel $\varepsilon^t_\parallel$ to the airway direction. The channel geometry (Fig. 2a) can be reduced to two relevant parameters in our minimal model: the relative channel height with respect to the total thickness of the sheet $\Psi = h/(h + 2e)$ and the in-plane channel density $\Phi = d/(d + d_w)$, where h, e, d, d_w are geometrical parameters of the structure (Fig. 2b). Balancing stresses and making simplifying assumptions (detailed in Supplementary Text and Supplementary Figure 2), the target strains are then deduced following Hooke's law:

$$\epsilon_\parallel^t = \frac{p}{E}\frac{\Psi\Phi}{1-\Psi\Phi}(1-2\nu) = 0$$

$$\epsilon_\perp^t = \frac{p}{E}(2-\Phi)\Phi\left(\frac{\Psi}{1-\Psi} - \frac{\nu\Psi\Phi}{1-\Psi\Phi}\left[1+\nu\left(\frac{1-\Phi}{\Phi(1-\Psi)}\right)\right]\right)$$

(1)

where E and ν are the Young modulus and Poisson ratio of the elastomer. We measured the target strains (Fig. 2b) by inflating a ring composed of only a few channels, therefore free of radial constraint. Within our crude hypotheses, the longitudinal strain is zero for $\nu = 1/2$ as expected for an incompressible elastomer and we do observe that the longitudinal strain is much smaller than the transverse strain. We can account for the evolution of the parameters (Ψ, Φ) due to the deformation of the channels under pressure, as described in the Supplementary Information and input the actual values in Equation 1. The resulting non-linear prediction for the target strain is in very good agreement with experimental data, without any fitting parameter as illustrated in Fig. 2b (note that the calculations remain within the framework of Hookean linear elasticity: material stiffening at large strain is not considered in this simplified model).

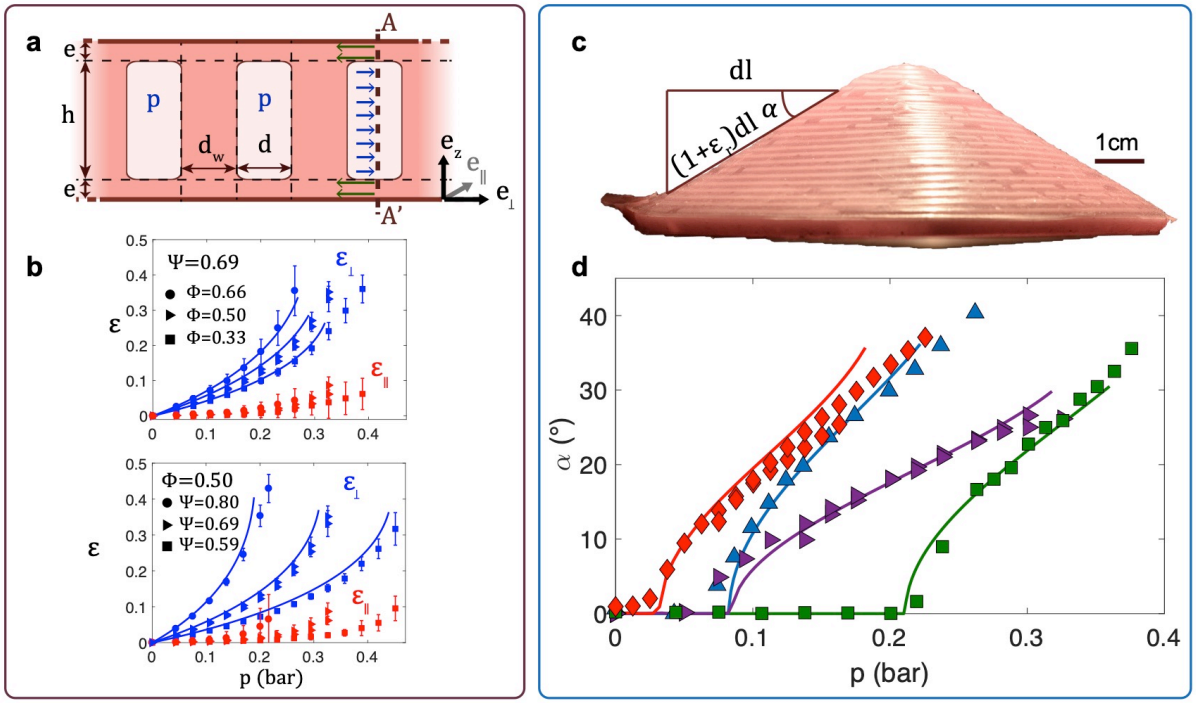

Figure2: Characterisation of baromorph expansion and deformation. **a**, Schematic vertical cut of the baromorph structure. The geometry of the channels can be reduced to two non- dimensional parameters: the relative height $\Psi = h/(h + 2e)$ and the channel density $\Phi = d/(d + d_w)$, where d is the width of the channels, d_w the width of the walls, h the height of the channels and e the thickness of the covering membrane. **b,** Dependence of the targeted parallel and longitudinal strain on the pressure for different values of Φ with $\Psi = 0.69 \pm 0.05$ and for different values of Ψ with $\Phi = 0.5 \pm 0.02$. Solid lines correspond to the model without any fitting parameter (in our simplified model ε∥ vanishes). **c,** Baromorph programmed to be a cone when pressurised. The slope angle is noted α. **d,** Experimental and theoretical (solid lines, no fitting parameter) evolution of α as a function of the applied pressure for baromorphs of different parameters: Red diamonds (Ψ = 0.78±0.05, Φ = 0.5, R = 50mm, H = 3.8±0.2mm); Blue triangles (Ψ=0.74,Φ=0.5,R=40mm,H=5.4mm); Purple flags (Ψ=0.68,Φ=0.2,R=50mm,H =6mm); Green squares (Ψ=0.6, Φ=0.5, R=40mm, H =6.7mm).

We now employ the concept of anisotropic target metric to program 3D shapes. As a first application, we target an axisymmetric shape, a cone. A configuration made of concentric and regularly spaced circular air channels is expected to induce a uniform radial target strain ε^t_r, while the azimuthal target strain remains null. Following elementary geometry (Fig. 2c), both target strains are satisfied if the airways keep their initial radii and the plate adopts a conical shape of slope α, with:

$$\cos\alpha = \frac{1}{1+\varepsilon_r^t} \qquad (2)$$

After a buckling transition, conical shapes with a tip regularised by the finite bending stiffness of the plate are observed for high-applied pressures (Fig. 2d, Supplementary Fig. 4). As in traditional buckling of slender structures, the finite bending stiffness of the plate indeed prevents out of plane buckling for small strains[24] (Supplementary Fig. 5). Both the buckling threshold and the evolution of the angle can be rationalised when inserting the incompatible target strain from Equation (1) within the Föppl-Von Karman equations for plates[25] (see Supplementary Text for a derivation and Supplementary Fig.3).

In Fig. 2d, results from numerical integration of these equations for incompatible plates without any fitting parameter are plotted in solid lines and match the experimental angles. Equation (1) is not limited to uniform channels, but is also valid locally if the channels distribution follows a gradient. In the configuration illustrated in Fig. 3, the channel density decreases with the radius, which results in a spiky structure when inflated. Conversely, the channels tend to collapse upon suction leading to a negative value of ε^t_r. As a consequence, the structure adopts a saddle shape with negative Gaussian curvature, as theoretically predicted by Efrati *et al.*[25]. A continuous family of shapes is thus obtained when adjusting the pressure. Each shape corresponds to an equilibrium state and can be easily reached on demand.

Another key advantage of baromorphs relies on their fast pneumatic actuation[26]. In the example described in Fig. 3c, a reversible transformation of the plate could be achieved with a frequency of 3 Hz (Supplementary Video 1). The structures presented in this study have an initial diameter on the order of 10 cm and channels of a section close to 1 mm^2. Baromorphs are however not limited to this size. For a given shape of the structure, the static mechanical response is independent of scale (Supplementary Figure 6 and Supplementary Video 2). Provided a sufficient power input, the actuation velocity is, in this case, limited by the natural frequency of the plate, $\omega \sim h(E/\rho)^{1/2}/R^2$, where ρ is the elastomer density, leading to a typical frequency of 10Hz. For small-scale structures, a poroelastic time scale could limit the actuation as in the context of water transport in plants[27]. Conversely, the finite compressibility of air may be a limiting issue for large baromorph structures. The actuation principle is moreover largely

material-independent, so that any elastomer may be used, including relatively stiff, tough and wear resistant rubber, allowing meter-sized structures to resist their weight.

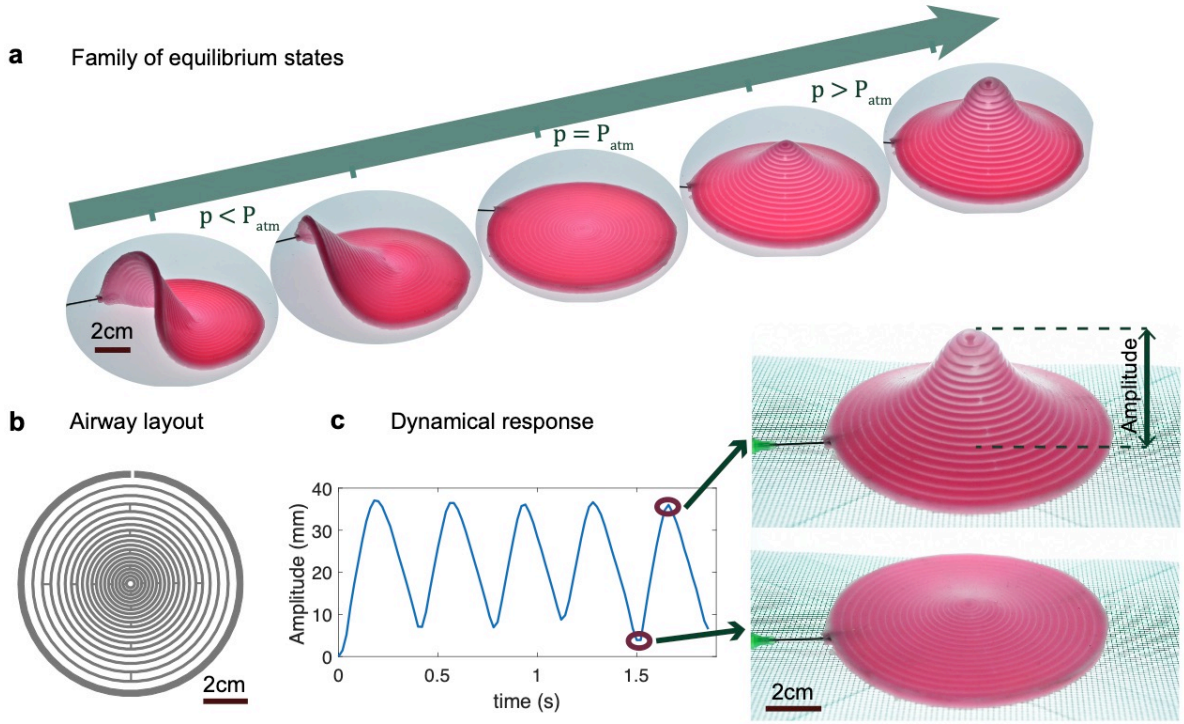

Figure 3: Equilibrium states and dynamical response. **a**, Continuous family of equilibrium states obtained for a baromorph at different pressures. **b**, Corresponding network of channels embedded in the plate. Channels are more concentrated in the central region of the disk, which leads to a spiky structure once inflated. **c**, Dynamical response: actuation at approximately 3Hz of The pneumatic system (Supplementary Video 6).

Having captured the mechanical ingredients involved in the transformation of a baromorph, we now explore shape-programming issues. Elementary shapes can be programmed through simple computations. For instance, purely radial or azimuthal growth of uniform intensity leads to a cone or an e-cone[11]. This is confirmed by baromorphs with entirely azimuthal (Fig. 4a) or radial channels (Fig. 4c) at constant channel density respectively, displaying zero Gaussian curvature except at the apex (see details on scanning technique in Methods and Supplementary Figure 1).

A spherical cap with constant positive Gaussian curvature (see Fig. 4b and Supplementary Video 3) is programmed by azimuthal channels with a density according to equation (2) with a varying value of angle $\alpha = \arcsin(r/R)$. As discussed in Supplementary information, less intuitive families

of shapes can be simply obtained from the azimuthal growth of radial channels. Surfaces with constant negative Gaussian curvature may be programmed with radial channels with varying density (Fig. 4d, Supplementary Video 4). Fig. 4e shows how a flat annulus almost becomes a cylinder, by expansion of the inner circumference (see Supplementary Fig. 7a and Supplementary Video 5). Baromorphs are not limited to axisymmetric plates. For instance, a ribbon may spontaneously buckle into a helicoid as expected when a larger target strain is programmed along the edges as illustrated in Fig. 4f (see Supplementary Fig. 7b and Supplementary Video 6).

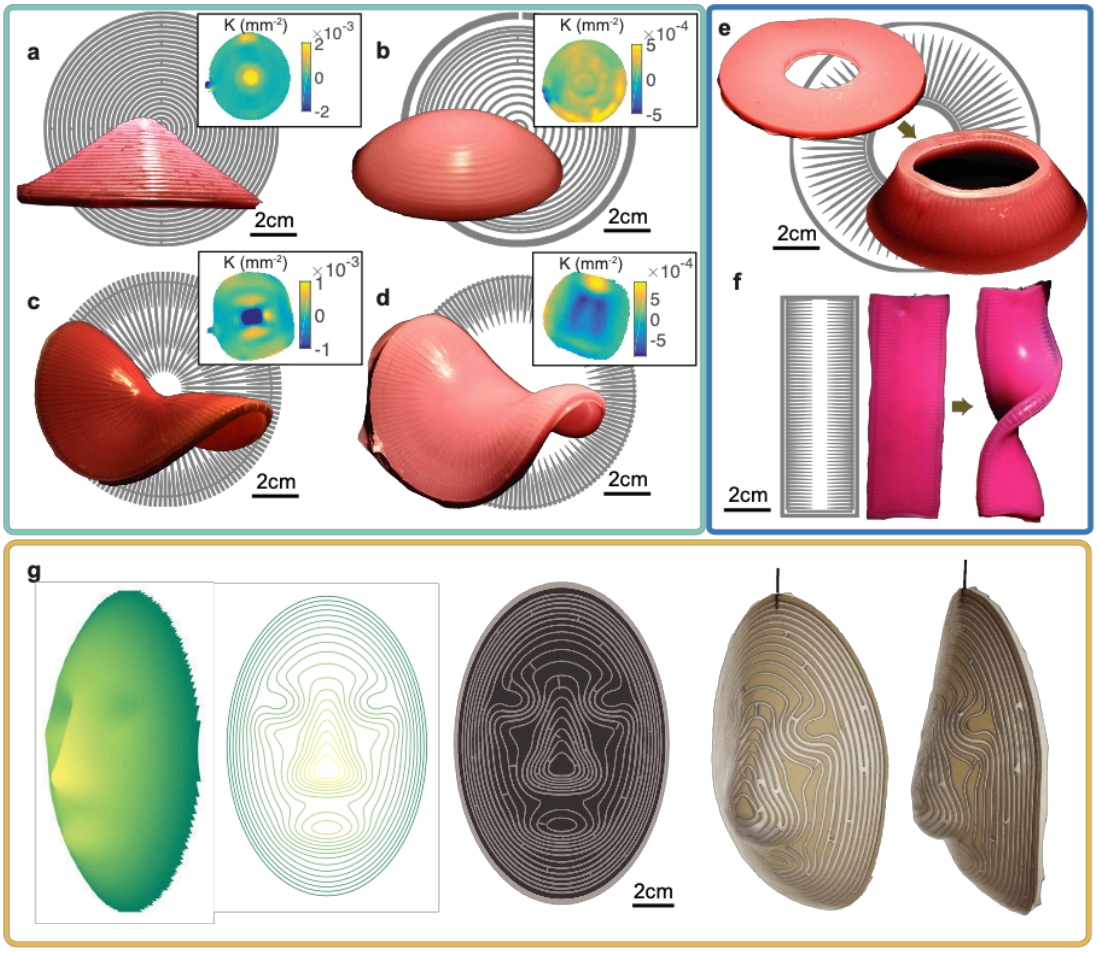

Figure 4: Collection of 3D shapes obtained by the buckling of baromorphs under pressure. Grey background paths represent the underlying airway network. Gaussian curvature K is plotted in insets. Circular concentric channels: cone (**a**) and portion of a sphere (**b**). Radial channels: e-cone (**c**) and saddle (**d**). **e**, Truncated cone of large angle. **f**, Helicoid . **g**, Shape programming of a face. From left to right: the target shape, the corresponding contour lines, the network of channels computed to give rise to the target metrics and two pictures of the deformed baromorph, made of Dragonskin 10 Medium from Smooth-On. Videos of the transformation of most structures are available as Supplementary Information (Videos 3-7).

Programming an arbitrary shape however involves a non-trivial inverse problem, as in other practical realisations of shape morphing. For instance, the direction of the anisotropic target growth (in nematic elastomers[8,28]), or the isotropic growth factor (in swelling gels[7] or auxetic materials[29]), corresponding to a given target shape may only be computed through a numerical optimisation procedure with no formal guarantee for the existence of a solution. In the specific case of baromorphs, the possibility to select both the orientation and the density of the channels enables us to tune at each point both the direction and intensity of the local expansion. Taking advantage of this additional degree of freedom, we propose a straightforward and intuitive analytical recipe for programming a smooth surface that can be parametrised as z = h(x, y). In this procedure, each point of the baromorph is moving along the z-axis during activation, in a simple generalisation of the axisymmetric case (Figure 2c).

Contour lines (curves with equal h projected onto the reference plane z = 0) are conserved in the process, and no growth occurs along these curves, which we choose as centreline for the baromorph channels. The local slope angle α measured on the target surface perpendicularly to the contour lines, tan α = ‖∇h‖, determines through Eq.(2) the lateral target strain

$$\epsilon_{\perp}^{t} = \sqrt{1 + \left(\frac{\partial h}{\partial x}\right)^{2} + \left(\frac{\partial h}{\partial y}\right)^{2}} - 1$$

(3)

which in turn sets the width of the airways, i.e. Φ, for the desired pressure p using Eq.(1).

This arrangement ensures that in the geometric limit, i.e. for thin enough plates, the baromorph will follow the target metrics (See Supplementary Text). Figure 4g shows the programming and the realisation of a face following the method described above. The results are qualitatively in good agreement with the target shape, except from the finest details, as the eyes, that are smoothed out by bending elasticity (Supplementary Video 7). Indeed, the size of the eyes is of the same order as the thickness of the sheet, and bending rigidity cannot be neglected at this scale.

Baromorphs constitute an efficient and versatile tool to transform 2D sheets into complex 3D structures reversibly with fast actuation. Numerous extensions of this architectured active material are possible for practical applications: cuts[29] can be made in the plate to release some bending constraints and improve the shape programming (Supplementary Figure 8 and Supplementary Video 8); the target curvature tensor can also be programmed[25, 30] using a bilayer composed of two independent networks of airways. In such a configuration, the homogenised sheet is free of constraint and the actuation does not involve any threshold. Snapping instabilities can also be triggered with out of phase actuation of the layers, as shown in Supplementary Video 9. More generally, several intertwined networks may be embedded in one plate to program various shapes on demand. Rather than simple channels, controlled cavities with different sizes and shapes may be embedded in the plate to impose all three components of the target growth tensor, in contrast with current morphing techniques[6, 7, 10, 28] (see Supplementary Figure 9 and Supplementary Video 10). Altogether, our study opens pathways in the numerous areas where shape morphing is believed to find new innovative applications, such as minimally invasive surgery, bio-printing, flow optimisation, architecture or more generally smart materials.

1. Ajaj, R. M., Beaverstock, C. S. & Friswell, M. I. Morphing aircraft: The need for a new design philosophy. *Aerospace Science and Technology* 49, 154 – 166 (2016).
2. Cianchetti, M. *et al.* Soft robotics technologies to address shortcomings in todays minimally invasive surgery: The stiff-flop approach. *Soft Robotics* 1 (2014).
3. Gao, B. *et al.* 4d bioprinting for biomedical applications. *Trends in Biotechnology* 34, 746 – 756 (2016). Special Issue: Biofabrication.
4. McEvoy, M. A. & Correll, N. Materials that couple sensing, actuation, computation, and communication. *Science* 347 (2015).
5. Shepherd, R. F. *et al.* Multigait soft robot. *Proceedings of the National Academy of Sciences* 108, 20400–20403 (2011).

6. Klein, Y., Efrati, E. & Sharon, E. Shaping of elastic sheets by prescription of non-euclidean metrics. *Science* 315 (2007).

7. Kim, J., Hanna, J. A., Byun, M., Santangelo, C. D. & Hayward, R. C. Designing responsive buckled surfaces by halftone gel lithography. *Science* 335, 1201–1205 (2012).

8. Aharoni, H., Sharon, E. & Kupferman, R. Geometry of thin nematic elastomer sheets. *Phys. Rev. Lett.* 113, 257801 (2014).

9. Erb, R. M., Sander, J. S., Grisch, R. & Studart, A. R. Self-shaping composites with pro- grammable bioinspired microstructures. *Nature communications* 4, 1712 (2013).

10. Sydney Gladman, A., Matsumoto, E. A., Nuzzo, R. G., Mahadevan, L. & Lewis, J. A. Biomimetic 4d printing. *Nature Materials* 15 (2016).

11. Dervaux, J. & Ben Amar, M. Morphogenesis of growing soft tissues. *Phys. Rev. Lett.* 101, 068101 (2008).

12. Rebocho, A. B., Kennaway, J. R., Bangham, J. A. & Coen, E. Formation and shaping of the antirrhinum flower through modulation of the cup boundary gene. *Current Biology* 27, 2610 – 2622.e3 (2017).

13. Nath,U.,Crawford,B.,Carpenter,R.&Coen,E.Geneticcontrolofsurfacecurvature, *Science* 299, 1404 (2003).

14. Fratzl, P., Elbaum, R. & Burgert, I. Cellulose fibrils direct plant organ movements. *Faraday Discuss.* 139, 275–282 (2008).

15. Armon, S., Efrati, E., Kupferman, R. & Sharon, E. Geometry and mechanics in the opening of chiral seed pods. *Science* 333, 1726–1730 (2011).

16. Reyssat, E. & Mahadevan, L. Hygromorphs: from pine cones to biomimetic bilayers. *Journal of The Royal Society Interface* 6, 951–957 (2009).
17. Pezzulla, M., Smith, G. P., Nardinocchi, P. & Holmes, D. P. Geometry and mechanics of thin growing bilayers. *Soft Matter* 12, 4435–4442 (2016).
18. Serikawa, K. A. & Mandoli, D. F. An analysis of morphogenesis of the reproductive whorl of acetabularia acetabulum. *Planta* 207, 96–104 (1998).
19. Huang, L. *et al.* Ultrafast digital printing toward 4d shape changing materials. *Advanced Materials* 29, 1605390–n/a (2017). 1605390.
20. Gorissen,B.*et al.* Elastic inflatable actuators for soft robotic applications. *Advanced Materials* (2017).
21. Pikul, J. H. *et al.* Stretchable surfaces with programmable 3d texture morphing for synthetic camouflaging skins. *Science* 358, 210–214 (2017).
22. Bertoldi, K., Vitelli, V., Christensen, J. & van Hecke, M. Flexible mechanical metamaterials. *Nature Reviews Materials* 2, 17066 (2017).
23. Timoshenko, S. & Woinowsky-Krieger, S. *Theory of plates and shells* (McGraw-Hill, 1959), 2n edition.
24. Dias, M. A., Hanna, J. A. & Santangelo, C. D. Programmed buckling by controlled lateral swelling in a thin elastic sheet. *Physical Review E* 84, 036603 (2011).
25. Efrati, E., Sharon, E. & Kupferman, R. Elastic theory of unconstrained non-euclidean plates. *Journal of the Mechanics and Physics of Solids* 57, 762–775 (2009).
26. Mosadegh, B. *et al.* Pneumatic networks for soft robotics that actuate rapidly. *Advanced Functional Materials* 24, 2163–2170 (2014).
27. Dumais, J. & Forterre, Y. Vegetable dynamicks: The role of water in plant movements. *Annual Review of Fluid Mechanics* 44, 453–478 (2012).
28. Aharoni, H., Xia, Y., Zhang, X., Kamien, R. & Yang, S. Universal inverse design of surfaces with thin nematic elastomer sheets. *Proc. Natl. Acad. Sci.* (2018).

29. Konakovic, M. *et al.* Beyond developable: Computational design and fabrication with auxetic materials. *ACM Trans. Graph.* 35, 1–11 (2016).
30. van Rees, W. M., Vouga, E. & Mahadevan, L. Growth patterns for shape-shifting elastic bilayers. *Proceedings of the National Academy of Sciences* (2017).

Methods

Making baromorph plates. Baromorph plates are made of polyvinyl siloxane (Elite Double 8 from Zhermack or Dragon Skin 10 Medium from Smooth-On) by mixing equal quantities of ”catalyst” and ”base” liquids. The mixture is then poured on a 3D printed mould designed using OpenScad software and printed with Form2 printer from Formlabs. If necessary, the whole setup is placed in a vacuum chamber to efficiently remove trapped air bubbles. Curing takes respectively 20 minutes and 3 hours. At the same time, a sheet of thickness e of the same elastomer is spread on a flat surface and cured. The structure removed from the mould is finally closed by ”gluing” the flat sheet on top of the moulded sheet using a thin layer of uncured mixture of the same material.

Experimental strain data. Azimuthal and radial strains are measured experimentally using DIC (Digital Image Correlation) program CorreliQ4 on Matlab[31]. A random pattern of dots is generated on the surface by spraying paint. Top view pictures of the baromorph structure are taken at different pressures and the program tracks in-plane strain with respect to a chosen reference image. Mean strains perpendicular and parallel to the channels are then extracted.

3D scanning and computation of Gaussian curvature. The surface topography of inflated baromorph structures was measured with a 3D scanning system developed in the laboratory and based on the work of Cobelli *et al.*[32]. Basically, the 3D shape is inferred from the distortion of a pattern of stripes projected on the structure (Supplementary Fig. 1ab). The local height is thus deduced from the phase shift of the periodic pattern.

Although Fourier transform is generally used to extract the phase, the lack of periodic boundaries prevented us from using this method. We instead used a phase shifting profilometry technique, detailed by Van der Jeught *et al.*[33]. Four patterns are successively projected and recorded with the camera, each time shifted by $\pi/2$. The local phase $\varphi(x, y)$ can thus be directly computed as:

$$\varphi(x, y) = \arctan\left(\frac{I_4 - I_2}{I_3 - I_1}\right) \quad (4)$$

where I_{1-4} is the local fringe intensities at pixel (x,y) for the different phase-shifted patterns. The local phase is defined at each pixel modulo π. It is then unwrapped using a 2D unwrap Matlab code written by Muhammad F. Kasim (2D Weighted Phase Unwrapping) based on the work of Ghiglia and Romero[34]. The local surface height can be deduced from phase shift with respect to reference image $\Delta\varphi(x, y)$ using basic geometrical optics:

$$h(x, y) = \frac{\Delta\varphi L}{\Delta\varphi - 2\pi D/t} \quad (5)$$

where $\Delta\varphi = \varphi(x, y) - \varphi_0(x, y)$, D is the distance between the video projector and camera, L is the height of both instruments with respect to the flat surface of reference and t is the spatial wave length of the fringed pattern (Supplementary Fig. 1c). The Gaussian curvature is finally deduced from a local quadratic fit of the surface (Supplementary Fig. 1d).

31. Hild, F. & Roux, S. Digital image correlation: from displacement measurement to identifica- tion of elastic properties–a review. *Strain* 42, 69–80 (2006).
32. Cobelli, P. J., Maurel, A., Pagneux, V. & Petitjeans, P. Global measurement of water waves by fourier transform profilometry. *Experiments in Fluids* 46, 1037 (2009).
33. der Jeught, S. V., Soons, J. A. M. & Dirckx, J. J. J. Real-time microscopic phase-shifting profilometry. *Appl. Opt.* 54, 4953–4959 (2015).

34. Ghiglia, D. C. & Romero, L. A. Robust two-dimensional weighted and unweighted phase unwrapping that uses fast transforms and iterative methods. *J. Opt. Soc. Am. A* 11, 107–117 (1994). 14

Acknowledgments This work has received the support of Institut Pierre-Gilles de Gennes (Équipement d'excellence, "investissements d'avenir", ANR-10-EQPX-34), and from ANR SMART. We thank Cyprien Blanquart for developing the 3D scanning technique and Mathias Lebihain from the Institut Jean Le Rond d'Alembert for the technical support on 3D printing the moulds.

Author contribution E.S. and B.R developed the baromorph concept. E.S. designed and conducted the experiments. E.S., E.R., J.B and B.R. analysed the data. E.S., J.B. and B.R. developed the theoretical model. All authors participated to the redaction of the manuscript.

Competing Interests The authors declare that they have no competing financial interests.

Data availability The authors declare that the data supporting the findings of this study are available within the paper and its supplementary information files and from the corresponding author upon reasonable request.

Correspondence Benoit Roman (email: benoit.roman@espci.fr).

Supplementary Information

Bio-inspired pneumatic shape morphing elastomers

Emmanuel Siéfert[1], Etienne Reyssat[1], José Bico[1], Benoit Roman[1]

[1]Laboratoire de Physique et Mécanique des Milieux Hétérogènes
CNRS, ESPCI Paris, PSL Research University, 10 rue Vauquelin, 75005 Paris, France,
and Sorbonne Universités, Université Paris Diderot

Contents

1 3D scanning and computation of Gaussian curvature

As explained in the *Methods* section of the paper, the surface topography of inflated baromorph structures was measured with a 3D scanning system developed in the laboratory and based on the work of Cobelli *et al.* [37]. The 3D shape is extracted from the distorsion of a pattern of fringes projected onto the structure (Supplementary Fig. 1ab). The local height is deduced from the phase shift of the periodic pattern, which enables one to reconstruct the 3D shape of the structure and the field of Gaussian curvature (Supp. Fig. 1cd).

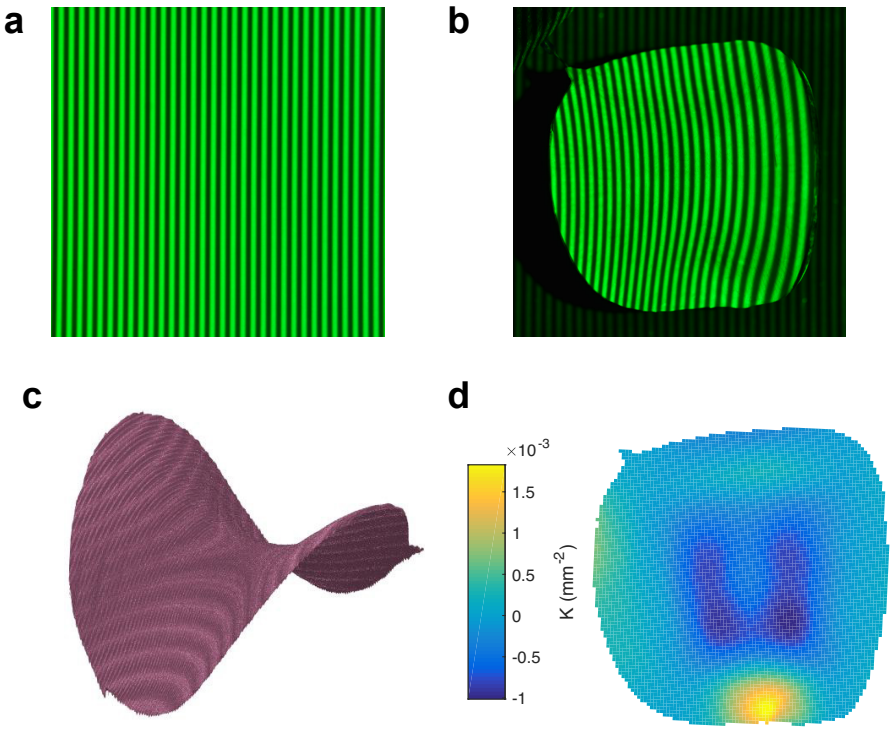

Supplementary Figure 1. 3D scanning technique. (see Methods) **a.** Picture of one of the four reference patterns projected on a white planar surface. **b.** Distorted pattern on the 3D surface of the baromorph. **c.** Reconstruction of the 3D surface with our program. **d.** Gaussian curvature computed with a local quadratic fit of the surface.

2 Theoretical framework

Target strain. We aim at modelling the in-plane target strains induced by the pressurization of the baromorph. We thus need to determine the whole stress distribution in the material. We respectively define $\Psi = h/(h+2e)$ and $\Phi = d/(d+d_w)$ as the relative channel height with respect to the total sheet thickness and the in-plane channel density (Supplementary Fig. 2). A cross-section of the plate is sketched in Supplementary Fig. 2. The membrane region at the top and at the bottom of the plate is denoted with the subscript (1).
A simple force balance reads:

$$\begin{cases} \sigma_{\perp}^{(1)} = p\dfrac{\Psi}{1-\Psi} \\ \sigma_{z}^{(1)} \sim 0 \end{cases} \tag{1}$$

We denote the region of the walls separating the channels with the subscript (2).
The force balance now leads to:

$$\begin{cases} \sigma_{\perp}^{(2)} = -p \\ \sigma_{z}^{(2)} = p\dfrac{\Phi}{1-\Phi} \end{cases} \tag{2}$$

To derive the average stress $\sigma_{\parallel}^{mean}$ in the direction $\mathbf{e}_{\parallel}$, we balance the force resulting from the pressure $hd\,p$ in one channel with the stress integrated on the complementary area $d_w(h+2e)+2ed$, which results into:

$$\sigma_{\parallel}^{mean} = p\frac{\Phi\Psi}{1-\Phi\Psi} \tag{3}$$

However, the distribution of $\sigma_{\parallel}$ in both regions remains undetermined. Nevertheless, the continuity of deformation along the direction of the channels imposes:

$$\epsilon_{\parallel}^{(1)} = \epsilon_{\parallel}^{(2)} \tag{4}$$

Following Hooke's law, we obtain:

$$\frac{1}{E}(\sigma_{\parallel}^{(1)} - \nu(\sigma_{\perp}^{(1)} + \sigma_{z}^{(1)})) = \frac{1}{E}(\sigma_{\parallel}^{(2)} - \nu(\sigma_{\perp}^{(2)} + \sigma_{z}^{(2)})) \tag{5}$$

where E and ν are the Young modulus and the Poisson coefficient, respectively. The material properties of our silicone elastomer are $E = 250 \pm 15\,\text{kPa}$ and $\nu = 1/2$.
We now assume that stresses along the channels in regions (1) and (2) are distributed according to their corresponding surface fraction, which leads to:

$$(1-\Psi)\sigma_{\parallel}^{(1)} + (1-\Phi)\Psi\sigma_{\parallel}^{(2)} = (1-\Psi\Phi)\sigma_{\parallel}^{mean} \tag{6}$$

We finally obtain a system of two equations and two unknowns that can be easily solved:

$$\begin{cases} \sigma_{\parallel}^{(1)} - \sigma_{\parallel}^{(2)} = \nu(\sigma_{\perp}^{(1)} + \sigma_{z}^{(1)} - \sigma_{\perp}^{(2)} + \sigma_{z}^{(2)}) \\ \\ (1-\Psi)\sigma_{\parallel}^{(1)} + (1-\Phi)\Psi\sigma_{\parallel}^{(2)} = (1-\Psi\Phi)\sigma_{\parallel}^{mean} \end{cases} \tag{7}$$

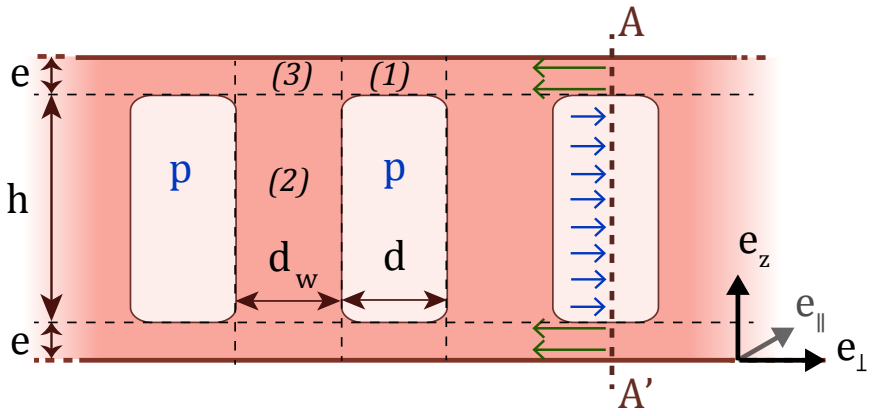

Supplementary Figure 2. Schematic cross section of a baromorph plate.

In terms of strain in the parallel direction, we obtain:

$$\begin{cases} \epsilon_{\parallel}^{(1)} - \epsilon_{\parallel}^{(2)} = 0 \\ (1-\Psi)\epsilon_{\parallel}^{(1)} + (1-\Phi)\Psi\epsilon_{\parallel}^{(2)} = \dfrac{p}{E}\Psi\Phi(1-2\nu) \end{cases} \tag{8}$$

It is remarkable to notice that for incompressible elastomers, the Poisson ratio is equal to $1/2$, which leads to $\epsilon_{\parallel}^{(1)} = \epsilon_{\parallel}^{(2)} = 0$. Knowing $\sigma_{\parallel}^{(1)}$ and $\sigma_{\parallel}^{(2)}$, we can now determine the strain in the other directions. Following Hooke's law, we get for region (i):

$$\begin{cases} \epsilon_{\perp}^{(i)} = \dfrac{1}{E}(\sigma_{\perp}^{(i)} - \nu(\sigma_{\parallel}^{(i)} + \sigma_z^{(i)})) \\ \epsilon_{\parallel}^{(i)} = \dfrac{1}{E}(\sigma_{\parallel}^{(i)} - \nu(\sigma_{\perp}^{(i)} + \sigma_z^{(i)})) = 0 \\ \epsilon_z^{(i)} = \dfrac{1}{E}(\sigma_z^{(i)} - \nu(\sigma_{\perp}^{(i)} + \sigma_{\parallel}^{(i)})) \end{cases} \tag{9}$$

Shear is finally not accounted for in our simplified model. Assuming that the strain in the upper part of the walls (region (3)) is the same as in the channel part (region (1)) is not reasonable. We thus propose to make the following assumption:

$$\epsilon_{\perp}^{(3)} \sim \Phi\epsilon_{\perp}^{(1)} \tag{10}$$

Indeed, in the two extreme cases, when Φ tends to 0, $\epsilon_{\perp}^{(3)}$ also approaches 0 and when Φ tends to 1, $\epsilon_{\perp}^{(3)}$ tends to $\epsilon_{\perp}^{(1)}$. The macroscopic homogenized radial strain is thus:

$$\epsilon_{\perp} = \Phi\epsilon_{\perp}^{(1)} + (1-\Phi)\epsilon_{\perp}^{(3)} \tag{11}$$

The homogenized strains parallel and perpendicular to the local channel direction thus read:

$$\begin{cases} \epsilon_{\parallel}^{t} &= \dfrac{p}{E}\dfrac{\Psi\Phi}{(1-\Psi\Phi)}(1-2\nu) = 0 \\ \\ \epsilon_{\perp}^{t} &= \dfrac{p}{E}\Phi(2-\Phi)\left(\dfrac{\Psi}{1-\Psi} - \dfrac{\nu\Psi\Phi}{1-\Psi\Phi}\left[1+\nu\left(\dfrac{1-\Phi}{\Phi(1-\Psi)}-1\right)\right]\right) \end{cases} \tag{12}$$

Note that both Ψ and Φ evolve with the pressure:

$$\begin{cases} \Phi = \dfrac{d(1+\epsilon_{\perp}^{(1)})}{d(1+\epsilon_{\perp}^{(1)}) + d_w(1+(\epsilon_{\perp}^{(2)}+\epsilon_{\perp}^{(3)})/2)} \\ \\ \Psi = \dfrac{h(1+\epsilon_{z}^{(2)})}{h(1+\epsilon_{z}^{(2)}) + 2e(1+\epsilon_{z}^{(1)})} \end{cases} \tag{13}$$

This dependence of the geometry with the pressure constitutes a key feature in inflation: as the pressure increases, the cross-section of the plate resisting the load is reduced, which results in concentrated stresses. This behaviour explains the non-linearity of the amplitude of the deformation with the pressure. We limit our simplified model to linear elasticity and do not account for the stiffening of actual elastomers. Such stiffening would tend to regularise the divergence of the strain at large pressures.

Bending and elongation stiffness of inflated baromorphs. Estimating the bending and stretching stiffness of an inflated baromorph structure is critical to compute its shape. Since bending a slender beam conserves the volume, this deformation does not involve any work of the inner fluid. As a consequence, the inner pressure only prevents failure of the thin membrane and should not affect the bending rigidity. However, inflating the structure tends to thicken it, which slightly increases the bending stiffness. We measured the shape of baromorph beams sagging under their own weight for different pressures (Supplementary Fig. 3a and b). The dependence on the pressure remains modest, as expected. Similarly, a stretching deformation conserves the volume in the solid ($\nu = 1/2$) as well as in the inner the fluid. As a result, the stretching stiffness should not change when the structure is stretched. A minor deviation from the ideal behaviour is however observed in Supplementary Fig.3c due to material stiffening under large strains.

Axisymmetric plate equations. Consider a flat circular baromorph, embedded with circular concentric channels of constant relative height Ψ. The channel density $\Phi(r)$ may vary along the radial direction.

The elastic energy stored in the plate corresponds to the sum of the stretching and bending energies:

$$U = U_{stretch} + U_{bend} \tag{14}$$

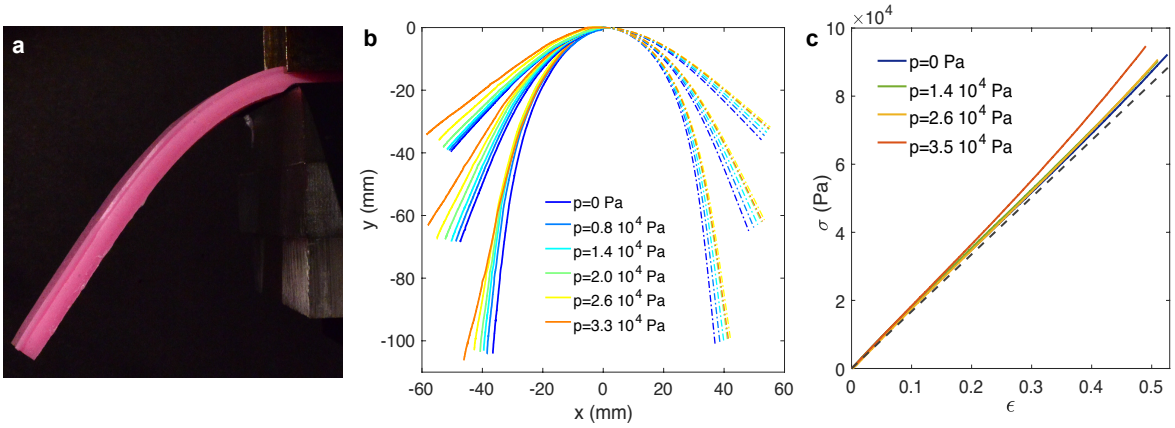

Supplementary Figure 3. Effect of the pressure on both bending and stretching stiffness of a baromorph cantilever beam for a fixed geometry ($\Phi = 0.5$, $\Psi = 0.69$, $H = 4.4\,\text{mm}$, $w = 30\,\text{mm}$). **a.** Picture of a baromorph cantilever bending under its own weight. **b.** Shape of a sagging beam for different clamping lengths and applied pressures. Experimental shapes (continuous lines on the left side) are compared with theoretical predictions (dashed lines on the right side). **c.** Engineering stress as a function of the strain for different applied pressures. The theoretical prediction is plotted as a dashed line.

with

$$U_{stretch} = \frac{1}{2}\iint \sigma : (\epsilon - \epsilon^t)\mathrm{d}S \tag{15}$$

$$U_{bend} = \frac{1}{2}\iint D(\kappa_1^2 + 2\nu\kappa_1\kappa_2 + \kappa_2^2)\mathrm{d}S \tag{16}$$

where D is the bending stiffness of the plate (assumed here isotropic for simplicity) and (κ_1, κ_2) are the principal curvatures of the plate. In the weak non-linear regime (within the limit of small slopes), the strain can be expressed at the second order in w' as:

$$\begin{cases} \epsilon_r = u' + \dfrac{1}{2}w'^2 \\ \\ \epsilon_\theta = \dfrac{u}{r} \end{cases} \tag{17}$$

where u and w correspond to the in-plane radial displacement and to the out-of-plane deflection, respectively. Using Hooke's law, we derive the stress distribution:

$$\begin{cases} \sigma_r = \dfrac{E(1-\Phi\Psi)}{1-\nu^2}\left(\epsilon_r - \epsilon_r^t + \nu(\epsilon_\theta - \epsilon_\theta^t)\right) \\ \\ \sigma_\theta = \dfrac{E(1-\Phi\Psi)}{1-\nu^2}\left(\epsilon_\theta - \epsilon_\theta^t + \nu(\epsilon_r - \epsilon_r^t)\right) \end{cases} \tag{18}$$

where, E is the Young modulus of the elastomer, ν the Poisson ratio of the material, ϵ_r^t and ϵ_θ^t are respectively the radial and azimuthal target strains computed in the previous section. We have assumed that the effective stretching stiffness of the plate is isotropic, which is not strictly true. Indeed, we expect the effective Young modulus to be $E(1-\Psi\Phi)$ in the azimuthal direction, where $(1-\Psi\Phi)$ corresponds to the proportion of material surface in a transverse cut. In the radial direction, we obtain for the effective modulus $E\left(1+\dfrac{\Psi\Phi}{1-\Psi}\right)$, by summing the compliance of the roof (region (1)) and the wall (region (2) and (3)). For typical values of $\Psi = 0.5$ and $\Phi = 0.66$, we estimate a difference of approximately 30% in stretching moduli. For the sake of simplicity, we thus use the value of the azimuths modulus for the other directions as well. The elastic stretching energy stored in the plate finally reads:

$$U_{stretch} = \frac{E\pi h}{1-\nu^2}\int_0^R (1-\Psi\Phi)\left[(u' + \frac{1}{2}w'^2 - \epsilon_r^t)^2 + 2\nu(u' + \frac{1}{2}w'^2 - \epsilon_r^t)\frac{u}{r} + (\frac{u}{r})^2\right] r\mathrm{d}r \tag{19}$$

We now focus on the bending energy. For an axisymmetric surface parametrised by $z = w(r)$, the two principal curvatures are determined by:

$$\begin{cases} \kappa_1 = \dfrac{w''}{(1+w'^2)^{3/2}} \\ \\ \kappa_2 = \dfrac{w'}{r\sqrt{1+w'^2}} \end{cases} \tag{20}$$

At the second order in w', the bending energy in the plate is given by:

$$U_{bend} = \frac{E\pi h^3}{12(1-\nu^2)}\int_0^R (1-\Phi\Psi^3)\left(rw''^2 + 2\nu w'w'' + \frac{w'^2}{r}\right)\mathrm{d}r \tag{21}$$

The total energy can be minimized with traditional variational methods, which leads to:

$$\begin{cases} w''' = \left(\dfrac{\Psi^3\Phi'}{1-\Psi^3\Phi} - \dfrac{1}{r}\right)w'' + \dfrac{w'}{r^2} + \dfrac{12}{H^2}\dfrac{1-\Psi\Phi}{(1-\Psi^3\Phi)}w'\left(u' - \epsilon_r^t + \dfrac{1}{2}w'^2 + \nu\dfrac{u}{r}\right) \\ \\ u'' = \epsilon_r^{t\prime} + \left(\dfrac{\Psi\Phi'}{1-\Psi\Phi} - \dfrac{1}{r}\right)u' + \dfrac{u}{r^2} - w''w' + \left(\dfrac{\Psi\Phi'}{1-\Psi\Phi} - \dfrac{1-\nu}{r}\right)\left(\dfrac{1}{2}w'^2 - \epsilon_r^t\right) \\ \qquad\qquad + \nu\epsilon_\theta^{t\prime} + \left(\nu\dfrac{\Psi\Phi'}{1-\Psi\Phi} - \dfrac{1-\nu}{r}\right)\epsilon_\theta^t \end{cases} \tag{22}$$

The relevant boundary conditions, i.e. no torque and no forces at the boundary of the plate,

correspond to:

$$\begin{cases} u(0) = 0 \\ \\ w'(0) = 0 \\ \\ u'(R) + \dfrac{1}{2}w'(R)^2 - \epsilon_r^t(R) + \nu\left(\dfrac{u(R)}{R} - \epsilon_\theta^t(R)\right) = 0 \\ \\ w''(R) + \nu\dfrac{w'(R)}{R} = 0 \end{cases} \tag{23}$$

This system of equations can be solved using the boundary value problem function bvp4c from Matlab. Results of the integration of these equations for uniform target strain configurations corresponding to various channel densities Φ and relative channel heights Ψ are presented in Supplementary Fig. 4 and in the Fig. 2 from the main body of the article. These predictions are in good agreement with our experiments without any fitting parameter.

Scaling law for buckling threshold. The buckling threshold leading to out-of-plane deformations can be roughly predicted by comparing stretching and bending energies in the flat and bent plate, respectively. We expect the transition to occur when bending gets energetically more favourable than in-plane strain.
In terms of scaling, the stretching energy $U_{stretch}$ is proportional to:

$$U_{stretch} \sim E\epsilon_r^2 H R^2(1 - \Phi\Psi) \tag{24}$$

where $H = h + 2e$ is the total thickness of the plate. Indeed if the plate remains flat, the azimuthal strain has to be of the same order of magnitude than the target radial strain (homothetic growth). Due to the presence of channels, the effective Young modulus in the azimuthal direction is now $E(1 - \Phi\Psi)$.
We expect the bending energy per unit length U_{bend} to scale as:

$$U_{bend} \sim EI\, R^2\kappa^2 \tag{25}$$

where EI is the effective bending rigidity of the homogenised plate and κ is the typical induced curvature. Considering the presence of the channels, we expect the effective bending rigidity in the azimuthal direction to scale as

$$I \sim H^3(1 - \Phi\Psi^3) \tag{26}$$

At the transition, radial strain and curvature are simply related by:

$$\epsilon_r \sim \kappa^2 R^2 \tag{27}$$

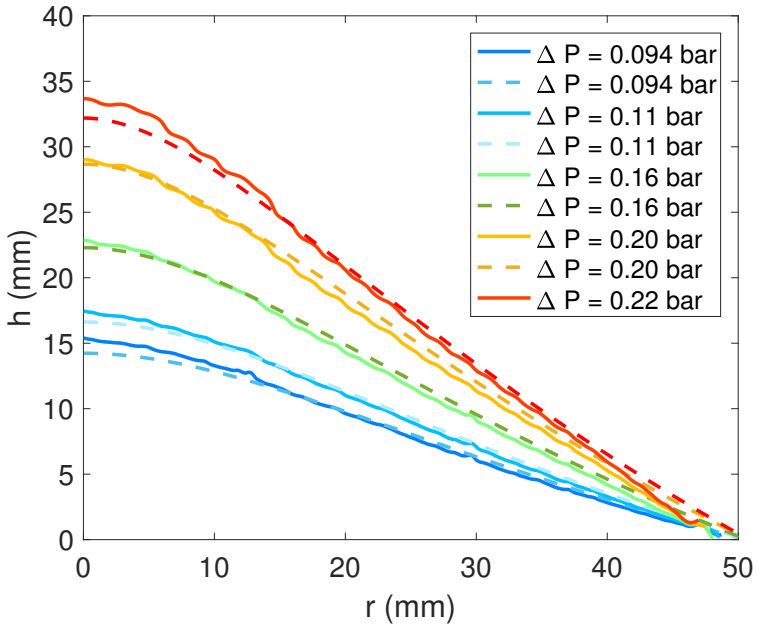

Supplementary Figure 4. Experimental (continuous lines) versus computed (dashed lines) cone profiles for various values of the applied pressure, with $\Phi = 0.5$, $\Psi = 0.75$, $R = 50\,\text{mm}$, $H = 4\,\text{mm}$

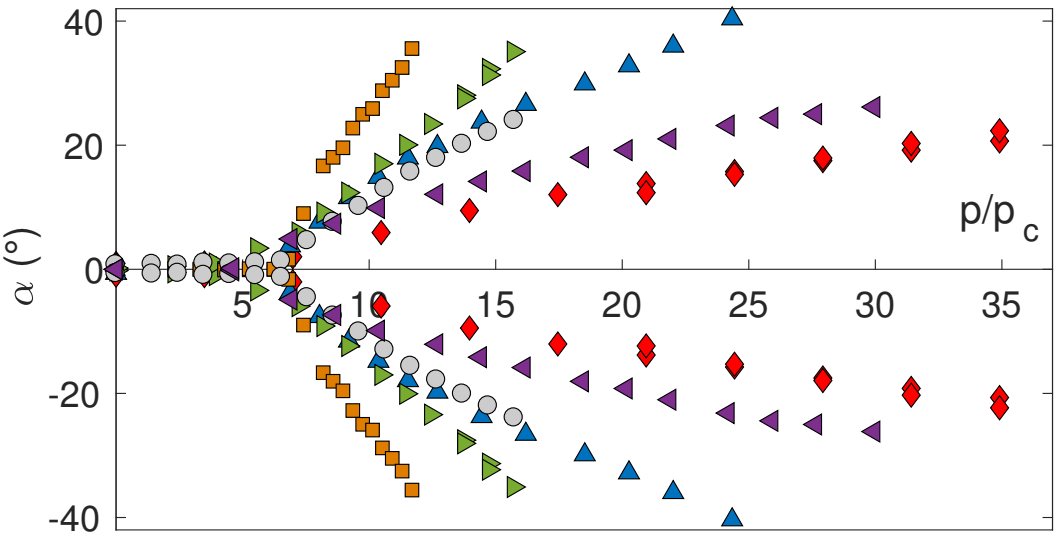

Supplementary Figure 5. Collapse of the instability threshold for various plates when pressure is rescaled by the typical critical pressure p_c from equation 30. Red diamonds ($\Psi = 0.78 \pm 0.05$, $\Phi = 0.5$, $R = 50\,\text{mm}$, $H = 43.8 \pm 0.2\,\text{mm}$); Blue triangles ($\Psi = 0.74$, $\Phi = 0.5$, $R = 40\,\text{mm}$, $H = 5.4\,\text{mm}$); Green flags ($\Psi = 0.67$, $\Phi = 0.5$, $R = 40\,\text{mm}$, $H = 6.0\,\text{mm}$); Orange squares($\Psi = 0.60$, $\Phi = 0.5$, $R = 40\,\text{mm}$, $H = 6.7\,\text{mm}$); Grey circles ($\Psi = 0.47$, $\Phi = 0.5$, $R = 50\,\text{mm}$, $H = 6.4\,\text{mm}$); Purple flags ($\Psi = 0.68$, $\Phi = 0.2$, $R = 50\,\text{mm}$, $H = 4.4\,\text{mm}$).

The buckling transition should correspond to $U_{bend} \sim U_{stretch}$, which leads for the critical strain:

$$\epsilon_c \sim \frac{H^2}{R^2} \frac{1 - \Phi\Psi^3}{1 - \Phi\Psi} \tag{28}$$

We remark that we obtain the typical critical buckling strain $(H/R)^2$ corrected by the geometry of the plate. Similarly to I beams, our plates are indeed relatively stiffer in bending than in compression in comparison with full plates, since material is concentrated far from the neutral plane. As shown in the body of the article, the strain dependence on pressure reads:

$$\epsilon_r \sim \frac{\Phi\Psi(2 - \Phi)}{1 - \Psi} \frac{p}{E} \tag{29}$$

which finally leads to the critical buckling pressure:

$$p_c \sim E \frac{H^2}{R^2} \frac{1 - \Psi}{\Phi\Psi(2 - \Phi)} \frac{1 - \Phi\Psi^3}{1 - \Phi\Psi} \tag{30}$$

Supplementary Figure 5 shows how the buckling threshold collapses for various plates on a single point when internal pressure is normalised by the critical pressure presented in Eq. 30.

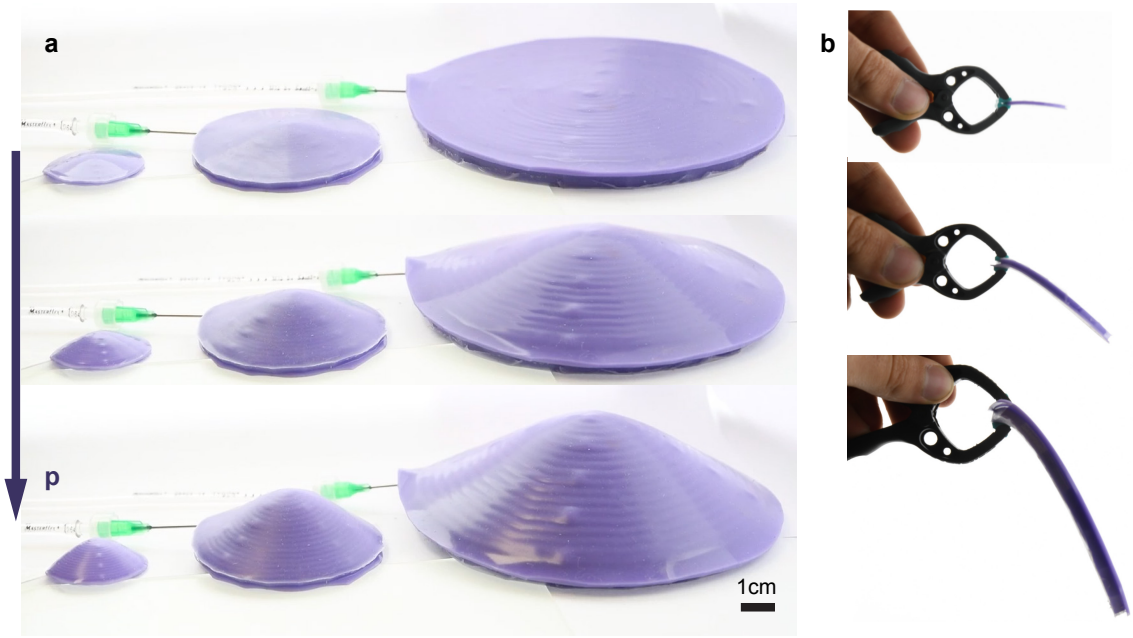

Supplementary Figure 6. Scalability of the baromorphs: **a.** Shape of structures (made of Elite Double 16 Fast from Zhermack) with the same design at different scales and three different pressures: $R = 15$ mm, $h = 1$ mm, $e = 0.4$ mm, $d = d_w = 0.4$ mm for the smallest sample, all dimensions multiplied by 2 and 4 respectively for the larger ones. (see Supplementary Movie 6). **b.** Deflection of the same baromorphs under gravity when clamped at one edge.

3 Scalability

From the mechanical point of view, when neglecting gravity forces, our system is scale free. As shown in the previous sections, stresses and deformations in the plate only depend on geometric parameters, Φ, Ψ - ratios between lengths- and a normalised pressure p/E. In order to highlight this property, we show in Supplementary Fig. 6a and Supplementary Movie 2 three baromorphs with the same design at three different scales allowed by the precision of the 3D printer, connected to only one pump. As the pressure is increased, all structures adopt the same shape, as predicted by our model.

Nevertheless, gravity forces do not have the same impact on all three objects. Indeed, the normalised deflection δ/R of a clamped baromorph scales as $\delta/R \sim \rho g R/(ES^2)$ in the small amplitude limit, where R is the radius of the baromorph and $S = h/R$ the slenderness ratio, kept constant. The larger the object is, the less it can sustain its own weight, as highlighted in Supplementary Fig. 6b. The maximum size of a baromorph which would sustain its own weight is given by a balance between the bending energy in the structure and the moment due to the gravity forces: $R_{max} \sim ES^2/(\rho g)$. This maximum size would be of the order of one meter for baromorphs made of elastomer of Young's Modulus of a few MPa and with a slenderness

ratio of 1:10. From a practical point of view, smaller baromorphs could be made using soft lithography techniques, down to the millimeter scale and beyond.

4 Shape Programming and inverse problem

Geometric procedure for the inverse problem. In this section, we propose a simple and intuitive strategy to program any 3D surface on a baromorph structure in the geometric limit, i.e., when the bending energy can be neglected with respect to the stretching energy. This strategy is a generalisation of the programming of a conical shape following Eq. 2 from the main text. Consider a given smooth surface parametrised by $z = h(x, y)$, that we want to reproduce, starting from a flat sheet. The first fundamental form reads:

$$\mathrm{ds}^2 = (1 + h_x^2)\mathrm{dx}^2 + 2h_x h_y \mathrm{dxdy} + (1 + h_y^2)\mathrm{dy}^2, \tag{31}$$

where h_x and h_y respectively correspond to $\partial h/\partial x$ and $\partial h/\partial y$. This first fundamental form can be written in the matrix form:

$$\overline{a} = \begin{pmatrix} 1 + h_x^2 & h_x h_y \\ h_x h_y & 1 + h_y^2 \end{pmatrix} \tag{32}$$

Diagonalising this matrix leads to the eigenvalues λ_1, λ_2 and corresponding eigenvectors $\mathbf{u}, \mathbf{v}$:

$$\begin{aligned} \lambda_1 = 1 \quad \mathbf{u} &= \frac{1}{\sqrt{h_x^2 + h_y^2}} \begin{pmatrix} -h_y \\ h_x \end{pmatrix} \\ \lambda_2 = 1 + h_x^2 + h_y^2 \quad \mathbf{v} &= \frac{1}{\sqrt{h_x^2 + h_y^2}} \begin{pmatrix} h_x \\ h_y \end{pmatrix} \end{aligned} \tag{33}$$

Interestingly, the fact that the first eigenvalue is equal to unity implies that there is no extension along isodepth lines with respect to a reference flat sheet. A natural idea is thus to draw channels along the contour lines projected on the reference plane, since no expansion parallel to the airways is predicted by our model. The second step consists in matching the target orthogonal strain to the metrics in the direction of the gradient:

$$\epsilon_\perp^t = \sqrt{\lambda_2} - 1 \tag{34}$$

According to our model, $\epsilon_\perp^t$ is a function of Ψ, Φ and p/E. Since airways are interconnected, p/E is uniform through the structure. In our manufacturing process, it is practically easier to tune the channel density Φ (i.e. the local channel width d) than the relative channel height Ψ. Equations (12) and (13) are thus solved using Matlab to find the relevant channel width to match the metrics along the gradient for fixed values of p/E and Ψ.
Following this concept, a simple code can automatically generate the airways path for any target 3D shape of the form $z = h(x, y)$. Nevertheless, the lateral expansion of the channels is limited by material properties ($\epsilon_{\perp\, max}^t \sim 2$). As a consequence, only surfaces with slopes smaller than typically 45° can be reproduced with this procedure.

Axisymmetric shapes In the case of an axisymmetric shape set by $z = h(r)$, this procedure leads to the target strains:

$$\begin{cases} \epsilon_\theta^t(r) = 0 \\ \\ \epsilon_r^t(r) = \sqrt{1 + h_r^2(r)} - 1 \end{cases} \tag{35}$$

For instance, in order to get a portion of a sphere of radius R as illustrated in Fig. 4b, the target radial strain should follow:

$$\epsilon_r^t(r) = \frac{1}{\sqrt{1 - \left(\frac{r}{R}\right)^2}} - 1 \tag{36}$$

Programming a shape with constant negative Gaussian curvature. Although the previous procedure could, in principle, be used to program shapes of negative Gaussian curvature such as saddles, edge effects tend to distort the resulting structures. We propose a different strategy to produce saddle shapes based on azimuthal expansion of circular plates.
The first fundamental form for a surface of constant negative Gaussian curvature K reads in cylindrical coordinates [33], $\mathrm{ds}^2 = \mathrm{dr}^2 - K^{-1}\sinh(r\sqrt{-K}))\mathrm{d}\theta^2$. Starting from a flat plate of first fundamental form $\mathrm{ds}^2 = \mathrm{dr}^2 + r^2 d\theta^2$, a straightforward solution to transform a circular plate in a saddle consists in keeping the distances in the radial direction unchanged and adapting the azimuthal expansion to the target metrics, $\epsilon_\theta^t = -r^2/6K + o(r^4/K^2)$. In our baromorphs, this strategy involves purely radial channels. For the sake of simplicity, we approximate the target azimuthal expansion by a constant piecewise function and compute the corresponding channel density required to achieve the target at one given pressure. Despite such approximations, the actual shape obtained is very close to the programmed saddle shape (See Fig. 4d from main text and Supplementary Movie 4), mainly because elasticity tends to smooth the programmed deformations. Particular attention should however be paid to the boundary effects in the plate: the additional wall necessarily present at the outer edge of the baromorph in order to seal the airways induces an additional resistance to expansion. It is thus necessary to design this wall as thin as possible in order to minimise its influence.

Other examples of lateral expansion: truncated cones and helicoids. Using the lateral expansion of radial channels is not limited to programming negative Gaussian curvature. We employed the same strategy to program truncated cones. Consider a circular plate with a central hole and radial channels (Fig. 4e from the main text and Supplementary movie 5). Applying an azimuthal strain while conserving radial distances also results in a new shape. In the geometric limit when bending stiffness can be neglected, we obtain the local angle from elementary geometry (Supplementary Fig. 7a):

$$\cos\alpha = 1 + \frac{\partial\, r\epsilon_\theta}{\partial r} \tag{37}$$

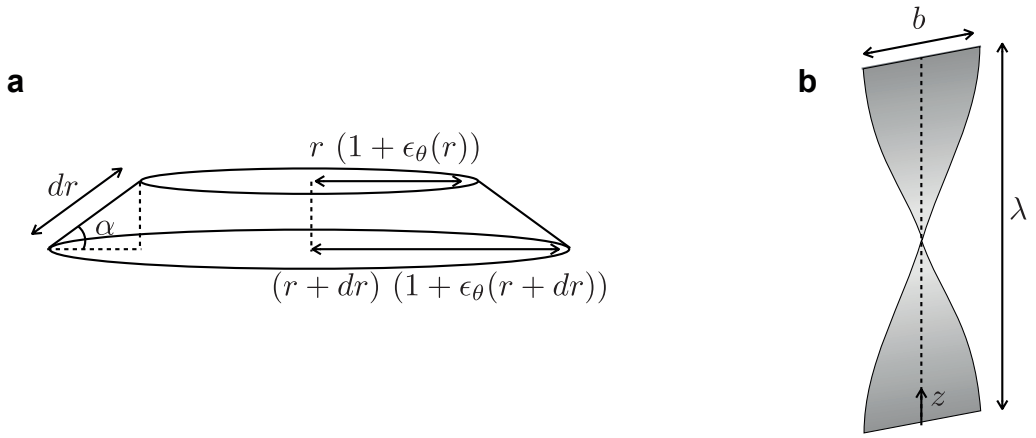

Supplementary Figure 7. a. Transformation of flat disk with a central hole based on azimuthal expansion (see also Fig. 4e and Supplementary movie 5). **b.** Twisting of a long rectangle into an helicoid by longitudinal extension along the edges (see also Fig. 4f and Supplementary movie 6).

The predicted shape is thus a truncated cone of angle α if the azimutal strain is of the form $\epsilon_\theta = \cos\alpha - 1 + A/r$. In practice, we approximate this form by a piece-wise function (fixed number of radial channels of uniform width in the inner part of the plate followed by a annular region without channels). The resulting shapes are in qualitative agreement with the prediction.

We also developed long rectangular plates with channels following a fish-bone design (Fig. 4f and Supplementary movie 6). Applying pressure thus tends to expand the edges of the rectangle, leading to a helical shape. If the width b and the length of the middle line of the rectangle are maintained constant, imposing a pitch λ results in a longitudinal strain (Supplementary Fig. 7b):

$$\epsilon_z = \left(\frac{4\pi^2 b^2}{\lambda^2} + 1\right)^{1/2} - 1 \tag{38}$$

The pitch obtained experimentally is in qualitative agreement with this relation.

5 A different shape-morphing strategy : baromorphs with cavities

Another possibility to achieve shape-morphing relies on non-uniform but isotropic growth: a hexagonal lattice of cylindrical bubbles interconnected by small channels is embedded in the elastomer plate. Similarly to Kim *et al.* halftone swelling technique [8], we take advantage of different local sizes of the cavities to induce a controlled isotropic expansion upon pressure: the bigger the cavities are, the larger the local "growth" is. In Supplementary Fig. 10, we highlight an example were cylindrical bubbles are larger in the centre than at the periphery of the plate, giving rise to positive Gaussian curvature once inflated.

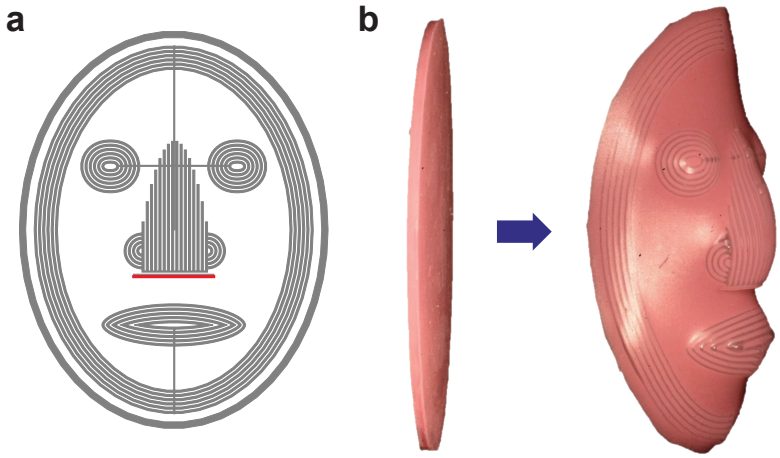

Supplementary Figure 8. Mask programmed with a cut : **a.** Network of airways embbeded in the plate, the red line highlighting the cut; **b.** Experimental shape transformation (see Supplementary Movie 6).

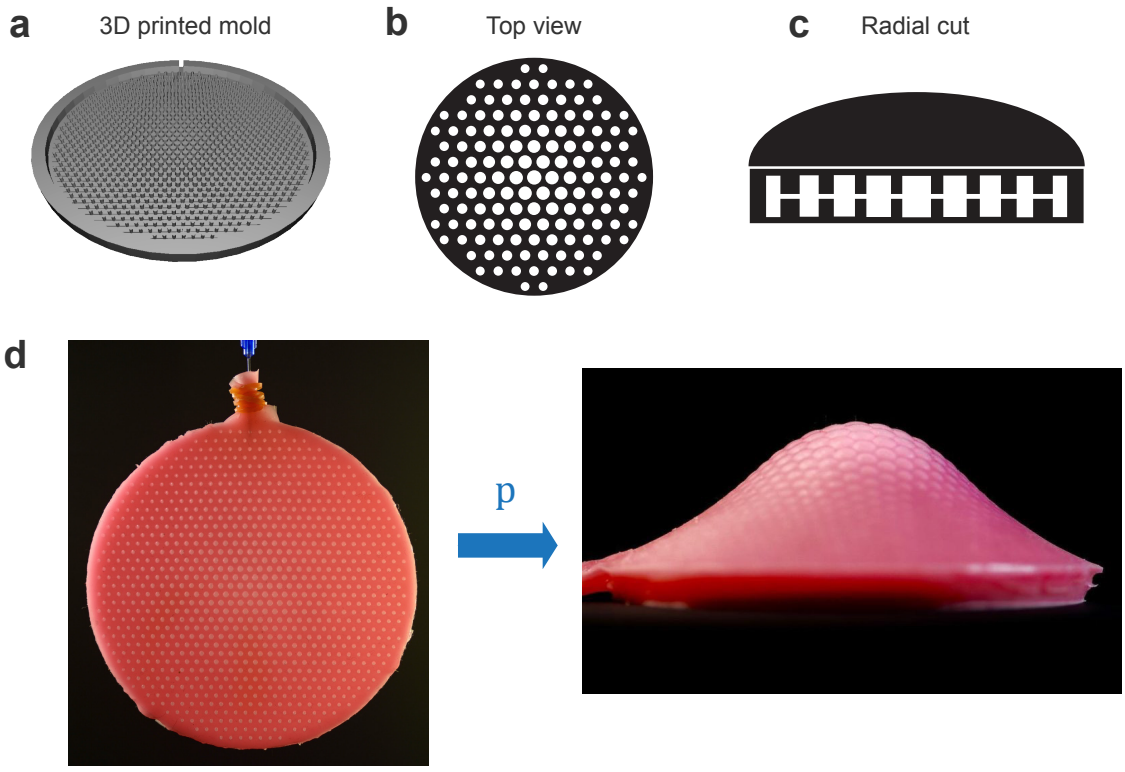

Supplementary Figure 9. Concept of isotropic baromorphs : **a.** 3D printed mould; **b.** schematic top view: a regular hexagonal lattice of cylinders of different radii; **c.** schematic radial cut of the isotropic baromorph: a small channel interconnects the cavities. **d.** pictures of the baromorph at rest and inflated (see Supplementary Movie 9).

6 Supplementary movies

Supplementary Movie 1
Dynamic behaviour of a baromorph under inflation and deflation.

Supplementary Movie 2
Parallel actuation of three baromorphs with the same design, at different scales.

Supplementary Movie 3
Bowl-shaped baromorph fitting a spherical cap.

Supplementary Movie 4
Saddle-shaped baromorph.

Supplementary Movie 5
Large angle cone with a centred hole.

Supplementary Movie 6
Helicoid obtained from a baromorph ribbon with a programmed elongation along the edges.

Supplementary Movie 7
Face programmed with the geometric inverse recipe.

Supplementary Movie 8
Mask with a cut below the nose.

Supplementary Movie 9
Actuation of a double layer baromorph. Stacking two structures provides some control on the curvature of the structure. Snapping instabilities can be observed when the applied pressures variations are out of phase.

Supplementary Movie 10
Actuation of an isotropic baromorph with larger cylindrical cavities in the centre of the plate than at the periphery.